Growing up in the city : a study of galaxy cluster progenitors at z>2

Kuiper, E.

7

Appendix: SINFONI results on individual galaxies in the Spiderweb

In this appendix we present additional results obtained with the SINFONI instrument of the Spiderweb galaxy at $z \sim 2.15$. Four protocluster galaxies are bright enough to study the emission line properties of individual pixels. We present velocity and linewidth maps for each of these galaxies. For those galaxies that show [OII], Hβ, [OIII] and Hα we also present line diagnostics that can be used to quantify dust extinction, ionising flux and metallicity. For the radio galaxy we find strongly disturbed internal dynamics, consistent with previous studies. We find tentative evidence that the central region of the radio galaxy is relatively unobscured and that dust attenuation becomes stronger further out from the centre. This is in sharp contrast with previous studies. The R_{23} value for the radio galaxy are uniformly larger than expected from photoionisation models, which may indicate that shocks are the principal means of ionisation in the radio galaxy. The other object which can be studied in great detail is located at a break in the radio jet (#10). The FWHM map shows possible evidence of an interaction between the jet and #10. We further find that this galaxy has little to no dust and $Z \sim \frac{1}{3} Z_{\odot}$. Further study is needed to draw conclusions from the figures presented here.

E. Kuiper
In preparation

7.1 Data

7.1.1 Integral field spectroscopy

We observed the Spiderweb galaxy and the surrounding field with the Spectrograph for INtegral Field Observations in the Near Infrared (SINFONI, Eisenhauer et al. 2003) on UT4 at the Very Large Telescope (VLT) on several nights in 2007 December and 2008 February. The field was observed in the J, H and K bands with extra focus on the H band.

SINFONI is a medium-resolution, image-slicing integral-field spectrograph that has a $8''\times8''$ field of view. A special dithering pattern was adopted to cover most of the central galaxies, leading to an effective field-of-view of approximately $15''\times15''$ centred on the radio galaxy. The spectral resolution of SINFONI varies among the three observed bands from $R = 2000$ in J to $R = 4000$ in K, corresponding to approximately $\Delta\lambda = 6$ Å.

Reduction of the data is summarized in Kuiper et al. (2011, Chapter 2) and is done in a method similar to the method described in Nesvadba et al. (2006) and Nesvadba et al. (2008). We refer to these works for further details.

7.1.2 Additional data

The SINFONI data is supplemented by deep Hubble Space Telescope (HST) data. These data were obtained with the Advanced Camera for Surveys (ACS, Ford et al. 1998) in the g_{475} and I_{814} bands (Miley et al. 2006) and with the Near Infrared Camera and Multi-Object Spectrometer (NICMOS) in the J_{110} and H_{160} bands (Zirm et al. 2008). Details on the data reduction can be found in these papers.

7.2 Results

7.2.1 Kinematics of individual objects

In Chapter 2 the redshifts of all protocluster candidates near the central radio galaxy have been determined. Here we go into more detail concerning the internal kinematics and emission line properties and diagnostics of the brightest of the protocluster galaxies. For all galaxies discussed here we set the systemic redshift to the redshift presented in Chapter 2. We also use the numbering adopted in that work. For clarity this numbering is shown in Fig. 7.1. Also, in all maps shown, North is up and East is to the left.

#1/the radio galaxy: The most prominent source of emission in each of the bands is the central radio galaxy itself. In Fig. 7.2 we show the full summed spectrum of the radio galaxy. The spectrum shows strong [OII], [OIII] and Hα lines that are due to its large star formation rate and the presence of an active supermassive black hole. In addition, several weaker emission lines can be seen as well. The J band spectrum shows the presence of the [NeIII]$\lambda3869, 3967$ doublet indicating hard ionisation possibly caused by shocks. Furthermore, a strong, but

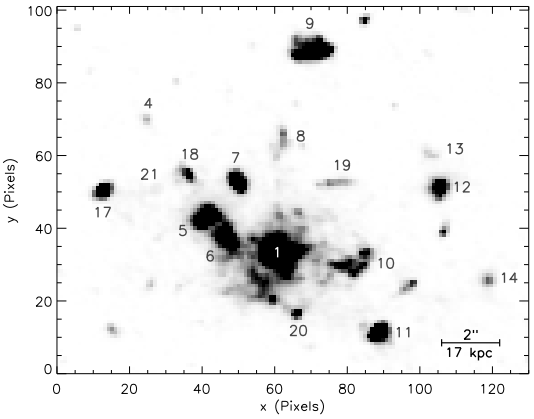

Figure 7.1 – Overview of the Spiderweb system. Image composed by coadding the g_{475}, I_{814}, J_{110} and H_{160} images. Numbers indicate the labeling used in this work.

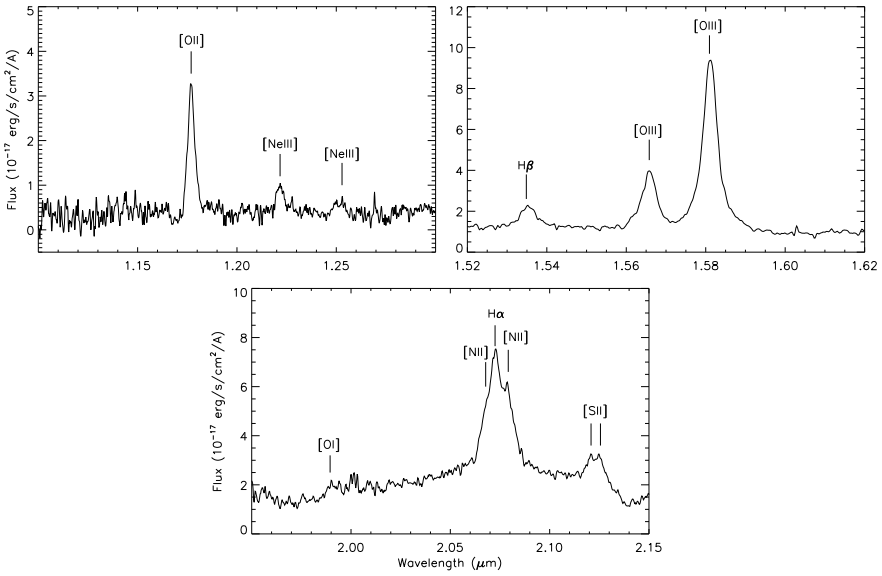

Figure 7.2 – Summed spectrum of the central radio galaxy in the J, H and K band.

unresolved [SII] doublet is present in K band. Finally, a weak feature can be seen at ~ 19900 Å that is consistent with being the [OI]λ6300 line. However, its location in the wings of the broad Hα feature makes it difficult to assess whether this feature is real. All three SINFONI bands also show stellar continuum emission from the radio galaxy. The data are not deep enough to identify stellar absorption lines.

The internal kinematics of the radio galaxy have been studied before in Nesvadba et al. (2006, hereafter N06). As is indicated by its disturbed continuum morphology, the kinematic structure of the radio galaxy is complex with evidence

for multiple outflowing 'bubbles'. The properties of these bubbles and the energy necessary to power them are consistent with being driven by the central AGN.

In the left column of Fig. 7.3 we show a series of three velocity maps based on the [OII], [OIII] and Hα emission lines. The [OII] and Hα velocity maps have been obtained by fitting the relevant emission line in each pixel with a single Gaussian. For the [OIII] emission line two Gaussians are used, because the complex kinematic structure leads to an additional [OIII] emission line in certain regions. Using a single Gaussian can result in ambiguity when determining the velocities if this additional emission feature is present. The velocities shown in the central panel of Fig. 7.3 denote the weighted mean of the individual velocities, with the fluxes of the individual lines acting as weights.

For all three bands the individual spectra are inspected visually in order to determine whether there is an emission line present and if so, whether it is fit properly. In addition, the panels in Fig. 7.3 show only those pixels with a fitted line flux at the $> 10\sigma$ level with respect to the rms noise. This is to ensure that the most uncertain pixels are removed from the maps.

The central panel, which is based on the [OIII] emission line, closely resembles the results obtained by N06. A strong redshifted outflow, corresponding to region 1 in N06, is seen to the East of the radio galaxy core, whereas a blueshifted region is seen to the West, corresponding to region 3 in N06. This general picture is also reflected in the Hα velocity map. The [OII] velocity map shows a lack of [OII] emission in the North-East region of the radio galaxy. This is the region that shows clear evidence for a high velocity outflow. Summing the J band spectra in this particular region we do find evidence for [OII] emission with a redshift of $z = 2.170$ or $\Delta v \sim +1000$ km s^{-1} with respect to the systemic redshift. This is consistent with the mean velocity of this particular region in the [OIII] velocity map.

The line width maps for the [OII], the [OIII] and the Hα line are shown in Fig. 7.3. The [OIII] FWHM map in the central panel shows a line width of 500-1000 km s^{-1} for large parts of the galaxy, but there are distinct regions with larger line widths up to 2000 km s^{-1}. These regions of larger line width are partially seen as well in the [OII] line width map. The Hα map in the bottom panel, however, shows larger FWHMs for almost the entire galaxy. This is due to the fact that the Hα line is blended with the [NII]$\lambda 6548, 6584$ doublet, thereby appearing broader. Regardless of this overall increase in the values for the FWHM, the Hα map still shows regions of relatively larger line width. These regions coincide roughly with the regions of increased FWHM seen in the [OIII] FWHM map.

Comparing the FWHM maps to the velocity maps of Fig. 7.3 it can be seen that the regions of large FWHM coincide with those regions that show large velocity gradients. This could indicate that the large FWHM regions are associated with the outflows.

The complexity of the kinematic structure is further illustrated in the spectra shown in Fig. 7.4. Five spectra are shown, each corresponding to a certain region

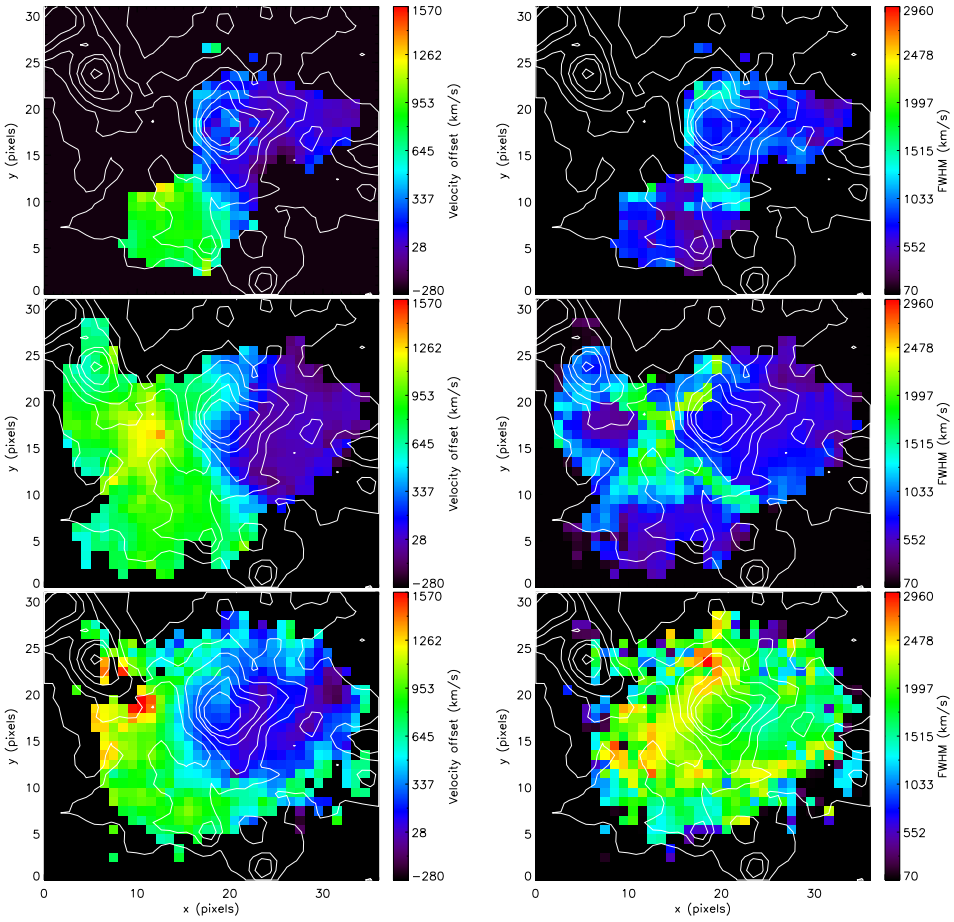

Figure 7.3 – Velocity and line width maps of the central radio galaxy in the left and right columns respectively. The maps have been made using, from top to bottom, [OII], [OIII] and Hα. White contours are obtained from the ACS I_{814} image.

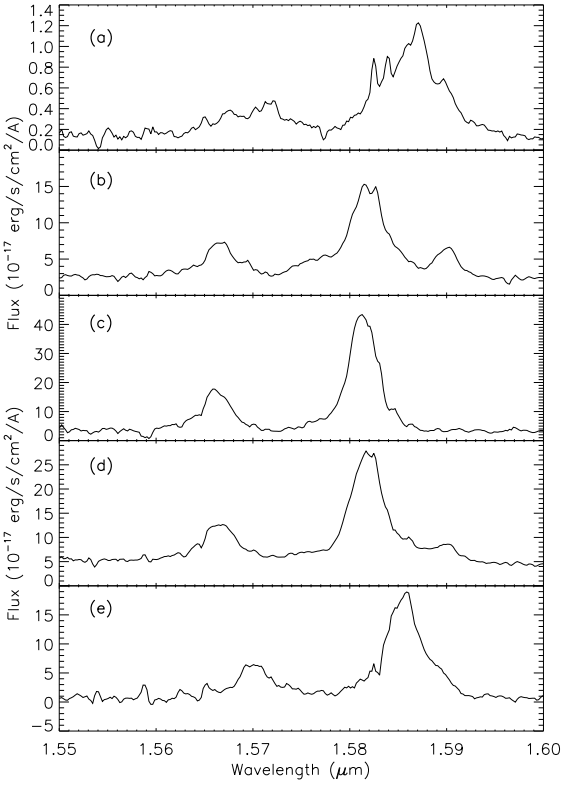

Figure 7.4 – Summed *H* band spectra of five distinct regions of the radio galaxy illustrating the complex kinematics of the galaxy. The regions are from top to bottom: East, North, West, central and South.

of the radio galaxy. Panel (c) shows the summed spectrum of the Western region which is largely blueshifted. This spectrum shows a regular [OIII] doublet without additional features. This is also the case for panel (e), which shows the southern region. Panels (a) and (b) show summed spectra of the Eastern and the Northern region, respectively. In panel (b) we see an additional emission feature redward of the main [OIII] emission line, the two of which have merged in panel (a). Panel (d) (the central region) also shows evidence of this additional, strongly redshifted [OIII] line.

The brightness of the radio galaxy allows us to study in some detail a number of line diagnostics that give information on a few galaxy properties. The ratio of Hα flux to Hβ flux, for instance, is a measure of extinction. This is given as

$$E(B-V) = \frac{2.5}{k(\mathrm{H}\beta) - k(\mathrm{H}\alpha)} \log\left(\frac{F_{\mathrm{H}\alpha}}{2.85 F_{\mathrm{H}\beta}}\right) \tag{7.1}$$

where 2.85 is the intrinsic ratio for Case B recombination (Osterbrock 1989) and $k(\mathrm{H}\alpha)$ and $k(\mathrm{H}\beta)$ are calculated using the Calzetti et al. (2000) extinction law. The resulting extinction map is shown in the left panel of Fig 7.5. Only those areas

are shown for which we are able to determine a robust Hβ flux. The map shows that the extinction in the radio galaxy is large, with $0.5 < E(B-V) < 1.5$. These values are likely overestimated due to the blending of Hα with the NII doublet.

It is interesting to note that the location with the largest line emission flux is also the location with the least extinction in the $E(B-V)$ map. The extinction at this location is $E(B-V) \sim 0.5$ mag. Going outward from this brightest pixel the extinction increases up to $E(B-V) \sim 1.3$ mag. This implies that the central regions of the radio galaxy are relatively unobscured in comparison with the outer regions.

For the regions that do not show significant Hβ emission it is difficult to assess how large the dust obscuration is. We try to estimate how large the dust extinction is by assuming a 3σ upper limit to the Hβ flux for those pixels that do not show Hβ emission. The FWHM values we assume are taken from the [OIII] linewidth map shown in Fig. 7.3. The resulting map is shown in the right panel of Fig. 7.5. There is a clear discontinuity between the region with 'accurate' $E(B-V)$ measurements and the region with Hβ upper limits, jumping from $E(B-V) \sim 1.0$ mag to $E(B-V) \sim 2.0$ mag. Since we consider Hβ upper limits, the $E(B-V)$ values are formally to be considered as lower limits. This implies that the discontinuity is even larger. However, the blending of Hα implies that the Hα flux is an upper limit further complicating the interpretation of the outer regions in terms of $E(B-V)$. If we consider an extreme contamination by [NII] and assume the flux ratio between Hα and [NII] is 1:1, then the $E(B-V)$ values in the maps would decrease by 0.6 mag. If we only apply this to the outer regions without Hβ emission, then $E(B-V)$ would decrease to ~ 1.5 mag. Therefore, the outer regions would still have larger extinction than the central regions. There is thus evidence that the outer regions of the radio galaxy are dustier than the inner regions. However, we must note that this can also be caused by a gradient in the contribution of the [NII] doublet to the Hα flux. If the contribution of the [NII] doublet is larger in the outer regions than in the central region, then there might not be any $E(B-V)$ gradient.

If there is such a gradient, then this is suprising. In Kurk (2003) a Lyα/Hα map was presented which showed a small line ratio of 0.09 at the core of the radio galaxy. This would indicate that the Lyα flux is strongly suppressed by possibly dust. However, based on the Hα/Hβ ratio we find evidence that the core should be relatively unobscured. Further study is necessary to explain this apparent discrepancy.

Another useful line diagnostic is R_{23} (Pagel et al. 1979) which is, in the absence of [OIII]λ4363, the best measure of metallicity. It is defined as

$$R_{23} = \frac{F_{[\mathrm{OII}]} + F_{[\mathrm{OIII}]\lambda 4959} + F_{[\mathrm{OIII}]\lambda 5007}}{F_{\mathrm{H}\beta}}. \tag{7.2}$$

The resulting R_{23} maps of the central region of the radio galaxy are shown in Fig. 7.6. The left and right panel show the R_{23} values obtained without and with correcting for dust extinction, respectively. These maps should therefore be

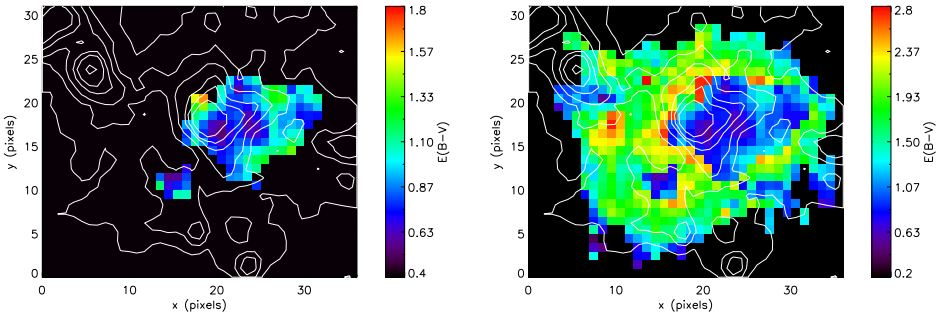

Figure 7.5 – Maps of colour excess $E(B-V)$ across the radio galaxy. The left panel shows the map for only those pixels with Hβ line emission. The right panel shows $E(B-V)$ values for all pixels with Hα emission and assumes upper limits for the Hβ emission. White contours are obtained from the ACS I_{814} image.

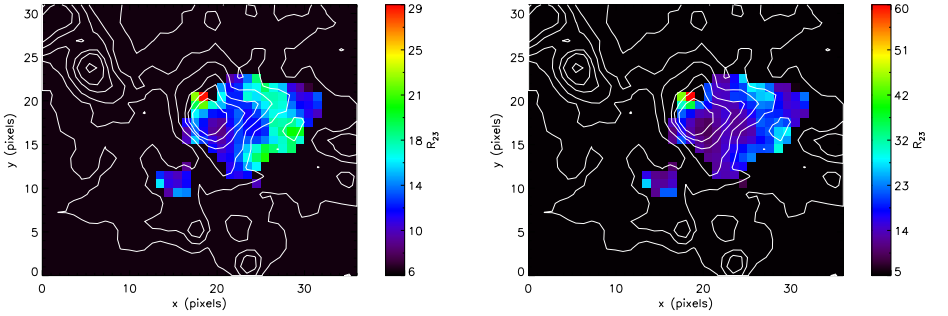

Figure 7.6 – Maps of the R_{23} ratio across the radio galaxy. In the left panel no correction for dust extinction is applied. For the right panel the relevant emission line fluxes are corrected for dust attenuation. White contours are obtained from the ACS I_{814} image.

considered the upper and lower limits to the true R_{23} values.

A similar trend is seen as in the $E(B-V)$ map: the central region has low R_{23} values of $\sim 10-15$ and this increases going out. There is also a small number of pixels with very large values for R_{23} in the North-East. These values are due to large dust extinction, strongly boosting the dust-corrected [OII] flux. In general, however, the R_{23} values in both maps are large. In low-z studies R_{23} is generally found to be < 12 (e.g. Nagao et al. 2006). High-z studies tend to find similar values (Maiolino et al. 2008). The majority of the pixels in both R_{23} maps show values > 12 and even exceeding $R_{23} = 15$. It therefore seems that even without reddening correction, the properties of the emission line gas in the radio galaxy are fundamentally different from that observed in local HII regions. It may be that, rather than photoionisation, the emission lines are caused by shock ionisation. Further study is needed to clarify this. Since the R_{23} maps show anomalously large values we cannot determine an actual metallicity.

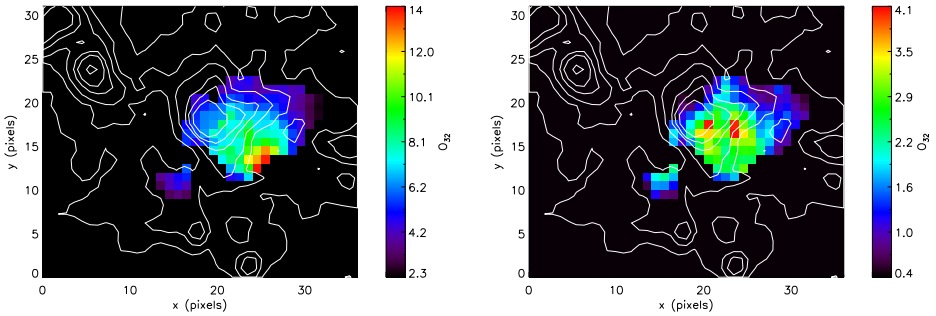

Figure 7.7 – Maps of the O_{32} ratio across the radio galaxy. The left and right panel show results with observed fluxes and dust-corrected fluxes, respectively. White contours are obtained from the ACS I_{814} image.

The final line diagnotic that we will consider is O_{32}. The O_{32} ratio is defined as the ratio between the total [OIII] and total [OII] flux. O_{32} is representative of the ionisation parameter U, because the lines are of the same element, but different ionisation states. Figure 7.7 shows the dust-uncorrected and dust-corrected O_{32} panels for the radio galaxy. Larger values of O_{32} correspond to a larger ionisation parameter: a larger number ionising photons. The ionisation parameter is found to be largest near the central regions. This is probably due to the powerful AGN at the centre of the galaxy. This region also hosts the [NeIII] lines seen in the left panel of Fig. 7.2. Being higher ionisation state lines, these features already indicate the presence of a large ionising flux.

#10: This is an interesting object due to its close proximity with respect to the main radio galaxy. It is located approximately $2''$ to the West of the radio galaxy. More importantly though, the radio jet originating from the central AGN shows a break at this exact location. The galaxy shows a large Lyα flux (Pentericci et al. 1997; Kurk 2003) and is also one of the brightest objects in the SINFONI data. In Chapter 2, its redshift was determined to be 2.1446 ± 0.0001 which is ~ 1300 km s^{-1} blueshifted with respect to the systemic redshift of the radio galaxy. Is it possible that the radio jet and the galaxy have a physical connection?

The velocity map of this galaxy is shown in the upper panel of Fig. 7.8 and is based on the [OIII] emission line. This is because the H band data is deepest and of the best quality. The [OIII] velocity map shows a smooth, but irregular velocity structure. The velocity structure can be divided into three general regions: redshifted motion in the east, blueshifted motion in the southwest and redshifted motion in the northwest. This division in three distinguishable regions is reminiscent of the UV continuum morphology which also shows three separate clumps. This is illustrated by contours in Fig. 7.8. These contours have been obtained from the g_{475} image. The pixel scale has been matched to the pixel scale of SINFONI, but the g_{475} image has not been smoothed to match the PSF of SINFONI. Doing this would result in the loss of the clumpy substructure. Nevertheless, even

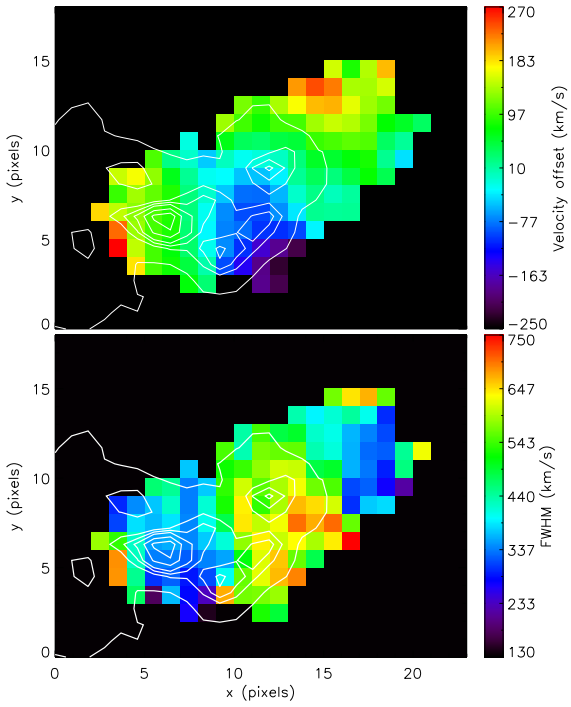

Figure 7.8 – Top panel and bottom panels show the velocity and linewidth map of satellite #10, respectively. Both maps have been made using the [OIII] emission line. White contours are obtained from the ACS g_{475} image.

though the PSFs do not match, the locations of the different regions in SINFONI match with distinct clumps in the continuum image. This indicates that the individual clumps are moving relative to each other with velocities of the order of ~ 200 km s^{-1}.

The division in different regions is also apparent in the linewidth map shown in the bottom panel of Fig. 7.8. Both of the redshifted regions show relatively small linewidths of 300-400 km s^{-1} whereas the southwest region shows larger linewidths of 500-700 km s^{-1}. The more turbulent gas is located at the approximate position of where the radio jet bends. This could be tentative evidence that there really is an interaction between the jet and the galaxy. However, this needs to be studied in more detail to draw any strong conclusions.

Since #10 shows a few additional emission lines, such as Hβ, we can check several line diagnostics as we have done for the central radio galaxy. However, galaxy #10 is substantially fainter than the central radio galaxy, severely limiting the number of pixels that show significant emission. Therefore we will limit our analysis to the average properties of the galaxy. In Fig. 7.9 we show the full summed spectrum of the galaxy. All pixels that show [OIII] emission have been included and individual spectra have been corrected to match the systemic redshift.

From the summed spectrum we find a small amount of dust extinction with $E(B-V) = 0.12$ mag. Hα cannot be distinguished from [NII], therefore the

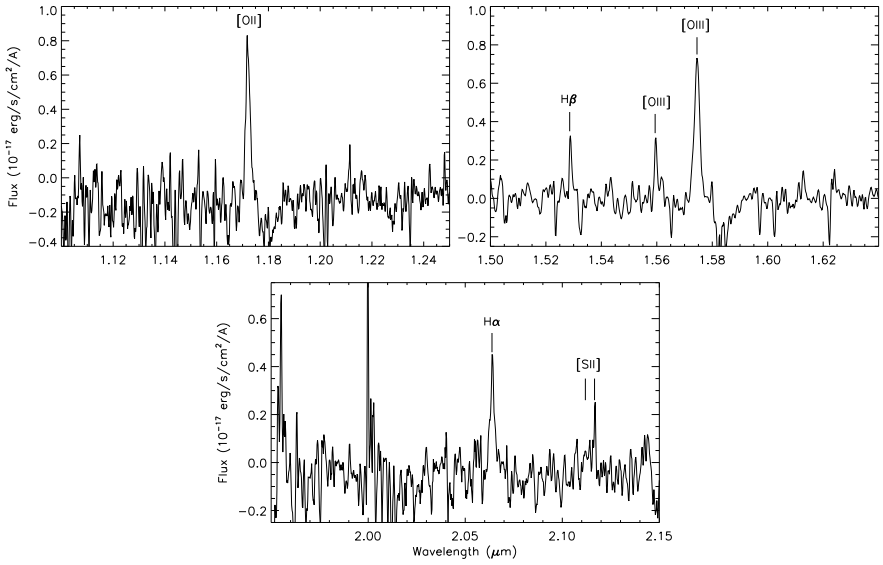

Figure 7.9 – Summed spectrum of galaxy #10. Main emission lines are marked.

Hα flux is likely overestimated. This in turn means that $E(B-V)$ should be considered an upper limit. There is thus very little dust attenuation in galaxy #10. This is consistent with the Lyα/Hα map of Kurk (2003), where a value of 11.3 was found. This is close to the value of 10 which is expected from case B recombination (Osterbrock 1989) and therefore consistent with little to no dust extinction. Ignoring any correction for dust, we find $R_{23} = 11.2$ and $O_{32} = 0.9$. In comparison to the radio galaxy, the R_{23} ratio of #10 is more in line with what is found for other galaxies.

Obtaining a metallicity from R_{23} is difficult due to the fact that R_{23} has a 'two-branch' degeneracy in metallicity and depends on the ionisation parameter U. We attempt to get an estimate of the metallicity by applying the upper branch parametrisation of Tremonti et al. (2004) and the lower branch parametrisation of Hu et al. (2009). The upper branch is given by

$$12 + \log(\mathrm{O/H}) = 9.185 - 0.313x - 0.264x^2 - 0.321x^3 \tag{7.3}$$

with $x \equiv \log R_{23}$ and the lower branch is given by

$$12 + \log(\mathrm{O/H}) = 6.45 + 0.15R_{23}. \tag{7.4}$$

This yields values of $12 + \log(\mathrm{O/H}) = 8.2$ and $12 + \log(\mathrm{O/H}) = 8.1$, respectively. R_{23} is thus such that the two metallicity branches almost meet and the degeneracy is not that strong. These values in turn convert to $\log(Z/Z_\odot) = -0.5$ and $\log(Z/Z_\odot) = -0.6$ using $\log(Z_\odot) = 8.69$ (Allende Prieto et al. 2001). These values are also consistent with the parametrisation of Maiolino et al. (2008) which is

based on $z > 3$ objects. The metallicity of galaxy #10 is therefore $\sim \frac{1}{3}\ Z_{\odot}$. Note that this is a very rough estimate and further study is needed to verify this value.

The O_{32} ratio found for #10 seems to fall at the lower end of what is found for the radio galaxy. The ionisiation parameter and the ionising flux therefore seem to be considerably smaller in #10 in comparison with the radio galaxy. Nevertheless, the galaxy still shows a remarkably large Lyα flux. The narrowband imaging of Pentericci et al. (1997) shows evidence that the extended Lyα halo of the system as a whole seems to have its peak flux at the location of #10 rather than the radio galaxy itself. Further research is needed to examine what this means in the context of the results presented here.

#12: This galaxy has an Hα narrowband excess indicating Hα line emission at the protocluster redshift. It was also selected as a protocluster candidate through its red colour (Hatch et al. 2009) and spectroscopically confirmed to be at the redshift of the radio galaxy in Chapter 2. In Fig. 7.10 the velocity and FWHM map are shown. Only maps obtained with the [OIII] line are shown as there is no indication of [OII] emission and the Hα emission is affected by poor night-sky transmission. This also means we will only present velocity and linewidth maps for this galaxy.

The velocity map shows a structure that may resemble a rotating disk, with redshifted motion on the top right and blueshifted motion on the bottom left of the galaxy. The FWHM maps, however, show a marked increase in the linewidth at the exact location of the blueshifted velocities. To determine whether this is truly a rotating disk an in depth kinemetry study is necessary (Krajnović et al. 2006; Shapiro et al. 2008). This is beyond the scope of this work.

#21: In Hatch et al. (2009) a bridge of red light was found between galaxies #17 and #18. The origin of the bridge of red light is unknown, but relatively strong line emission is found in the H band at the approximate location of this bridge. In Chapter 2 this was identified as being [OIII] at $z = 2.1505 \pm 0.0010$. No [OII] or Hα emission is found to verify this. The velocity and FWHM maps of the bridge are shown in Fig. 7.11.

The velocity map shows a clear bimodal velocity distribution with blueshifted emission in the West and redshifted emission in the East. The blueshifted clump coincides with the peak of the H band emission, whereas the redshifted line emission is in an arc and does not show any clear spatial correlation with the continuum flux. The two clumps are shifted ~ 800 km s^{-1} with respect to each other. Furthermore, there is no velocity gradient in either of the clumps which would indicate a continuous velocity variation between the clumps.

Hatch et al. (2009) hypothesised that the red light comes from gas that is gas being stripped from a merging system. This would imply that both #17 and #18 are protocluster galaxies as well even though no evidence for this can be found. An alternative possibility is that this is a heavily obscured galaxy, with all UV radiation being extinguished by large amounts of dust. If this is the case, one may expect some emission at longer wavelengths. Therefore we have visually

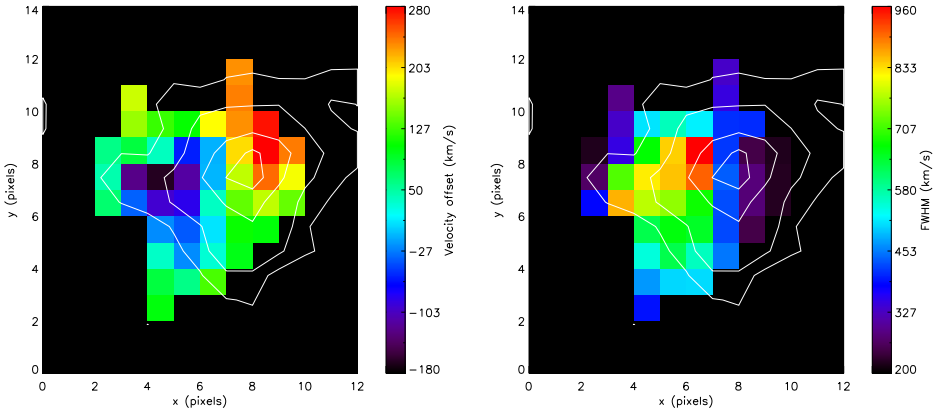

Figure 7.10 – Velocity and FWHM maps of satellite #12 in the top and bottom panel, respectively. Both maps are obtained using the [OIII] emission line. White contours are obtained from the NICMOS H_{160} image.

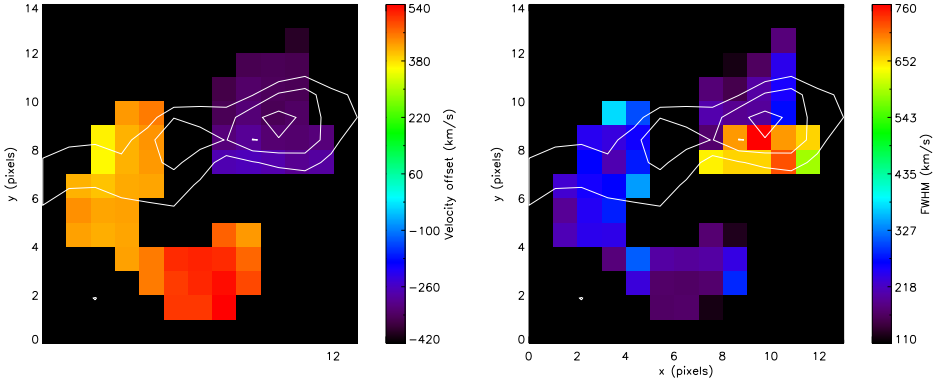

Figure 7.11 – Velocity and FWHM maps of satellite #21. White contours are obtained from the NICMOS H_{160} image.

investigated Spitzer images at 3.6-24 μm for traces of restframe optical emission (Audrey Galametz, private communication). However, the crowded nature of the field, the brightness of the radio galaxy and the relatively poor spatial resolution of the Spitzer images make it difficult to find strong evidence for this. Considering the large velocity difference between the two clumps, it may be that this is the result of a strong outflow. More data is needed to verify this. The nature of the line emission of #21 thus remains unknown for now.

References

Allende Prieto C., Lambert D. L., Asplund M., 2001, ApJ, 556, L63
Calzetti D., Armus L., Bohlin R. C., Kinney A. L., Koornneef J., Storchi-Bergmann T., 2000, ApJ, 533, 682
Eisenhauer F. et al., 2003, in Presented at the Society of Photo-Optical Instrumentation Engineers (SPIE) Conference, Vol. 4841, Society of Photo-Optical Instrumentation Engineers (SPIE) Conference Series, M. Iye & A. F. M. Moorwood, ed., pp. 1548–1561
Ford H. C. et al., 1998, in Society of Photo-Optical Instrumentation Engineers (SPIE) Conference Series, Vol. 3356, Society of Photo-Optical Instrumentation Engineers (SPIE) Conference Series, Bely P. Y., Breckinridge J. B., eds., pp. 234–248
Hatch N. A., Overzier R. A., Kurk J. D., Miley G. K., Röttgering H. J. A., Zirm A. W., 2009, MNRAS, 395, 114
Hu E. M., Cowie L. L., Kakazu Y., Barger A. J., 2009, ApJ, 698, 2014
Krajnović D., Cappellari M., de Zeeuw P. T., Copin Y., 2006, MNRAS, 366, 787
Kuiper E. et al., 2011, MNRAS, 415, 2245
Kurk J. D., 2003, PhD thesis, Leiden University, P.O. Box 9504, 2300 RA Leiden, The Netherlands
Nagao T., Maiolino R., Marconi A., 2006, A&A, 459, 85
Maiolino R. et al., 2008, A&A, 488, 463
Miley G. K. et al., 2006, ApJ, 650, L29
Nesvadba N. P. H., Lehnert M. D., De Breuck C., Gilbert A. M., van Breugel W., 2008, A&A, 491, 407
Nesvadba N. P. H., Lehnert M. D., Eisenhauer F., Gilbert A., Tecza M., Abuter R., 2006, ApJ, 650, 693
Osterbrock D. E., 1989, Astrophysics of gaseous nebulae and active galactic nuclei, Osterbrock, D. E., ed.
Pagel B. E. J., Edmunds M. G., Blackwell D. E., Chun M. S., Smith G., 1979, MNRAS, 189, 95
Pentericci L., Roettgering H. J. A., Miley G. K., Carilli C. L., McCarthy P., 1997, A&A, 326, 580
Shapiro K. L. et al., 2008, ApJ, 682, 231
Tremonti C. A. et al., 2004, ApJ, 613, 898
Zirm A. W. et al., 2008, ApJ, 680, 224